

Magnetic orders in the hole doped three-band Hubbard model: spin spirals, nematicity, and ferromagnetic domain walls

Adam Chiciak,¹ Ettore Vitali,¹ Hao Shi,^{1,2} and Shiwei Zhang¹

¹*Department of Physics, The College of William and Mary, Williamsburg, Virginia 23187*

²*Center for Computational Quantum Physics, Flatiron Institute, 162 5th Avenue, New York, New York 10010*

The Copper-Oxygen planes in cuprates have been at the center of the search for a theory of high-temperature superconductivity. We conduct an extensive study of the ground state of the three-band Hubbard (Emery) model in the underdoped regime. We focus on the magnetic and charge orders, and present results from generalized Hartree-Fock (GHF) calculations. The ground-state properties at the thermodynamic limit are challenging to pin down because of sensitivity to computational details including the shapes and sizes of the supercells. We employ large-scale computations with various technical improvements to determine the orders within GHF. The ground state exhibits a rich phase diagram with hole doping as the charge transfer energy is varied, including ferromagnetic domain walls embedded in an antiferromagnetic background, spin spirals, and nematic order.

I. INTRODUCTION

Despite more than thirty years of intense theoretical^{1–12} and experimental^{13–23} efforts, understanding high temperature superconductors has remained a major challenge. Significant progress has been made^{24–26} (see, e.g. Refs 22–24 for some reviews). The advent of petaflop computing and the emergence of new and improved computational methods have created unprecedented opportunities for the computational study of these exciting systems.

It is widely believed that the physical mechanism underlying high temperature superconductivity of the cuprates arises in the quasi-two-dimensional physics in the copper-oxide planes²⁷, with the other layers of the materials playing the role of charge reservoirs that can chemically dope the planes by adding or removing holes. Starting from a parent compound (zero doping) which is an antiferromagnetic insulator²⁸, the antiferromagnetism rapidly melts as holes are added, giving rise to a rich phase diagram where charge and spin orders appear to coexist, cooperating or competing^{26,29} with d-wave pairing superconducting order. A crucial question, naturally, is the following: what is the best model that captures the most important physics while being simple enough to allow theoretical and computational approaches to provide accurate answers?

The majority of recent theoretical efforts to study these planes have focused on the Hubbard hamiltonian³⁰ which, in the realm of high temperature superconductivity, is a low energy effective model that relies on the Zhang–Rice singlet notion³¹. These studies assume that the explicit contribution of the oxygen degrees of freedom can be neglected. Although impressively accurate results³² have been obtained on the one-band Hubbard model and very interesting magnetic and charge orders have emerged which reproduce some important experimental results, there are indications that the model, at least at zero temperature, does not allow a superconducting phase to become stable in the experimentally relevant regions of the parameter space (The t–J model, although

closely related, can contain different physics^{33–36} from the one-band Hubbard model with “physical” parameters for the interaction strength).

Moreover, recent x-ray scattering and nuclear magnetic resonance experiments seem to indicate that spin and charge density waves involve the Oxygen *p*-bands in a non-trivial manner^{17–21}. This suggests that one important direction to build a model that captures the physics of the cuprates may be the implicit or explicit inclusion of the Oxygen orbitals.

With advances in computational resources, it is now viable for a variety of methods to go beyond the one-band Hubbard model and treat the more realistic, three-band Hubbard model, known as the Emery model²⁷, which explicitly includes the Copper $3d_{x^2-y^2}$ and the Oxygen $2p_x$ and $2p_y$ orbitals. The Hamiltonian contains a set of parameters, including charge transfer energy, hopping amplitudes and on-site repulsion energies, which can in principle be computed with *ab initio* approaches, resulting in standard parameter sets for the cuprates.

However, the actual choice of the parameters is subtle. In particular, the value of the charge-transfer energy, $\Delta \equiv \epsilon_p - \epsilon_d$, can be affected by double-counting issues³⁷ in the computation. Empirically, the value of Δ appears to vary across different families of cuprates, controlling the density of holes around Copper and Oxygen atoms, and there are indications from experiment that it is correlated, or more precisely anticorrelated, with the critical temperature^{18,19,22,23}. Recently we have seen from quantum Monte Carlo calculations that the properties of the undoped, parent system can vary fundamentally with Δ ³⁸.

The prominent role of the parameter Δ motivated us to scan its values here and investigate the effects on the physical properties. The role of the charge-transfer energy has been investigated theoretically using cluster dynamical mean field theory³⁹, where the pairing order was addressed. Here we focus on spin and charge orders in the underdoped regime, which play an integral role in understanding the origin of superconductivity and potentially how to optimize the critical temperature T_c .

Although several studies addressed the behavior of the Emery model using different methodologies, including exact diagonalization of small clusters⁴⁰, random phase approximation⁴¹, embedding methodologies^{42,43}, quantum Monte Carlo^{44–47} and Density Matrix Renormalization Group⁵, comprehensive knowledge of the ground-state phase diagram, especially a full analysis of the role of Δ in determining the properties of the model, is still missing.

Since the phase diagram in the underdoped regime is intrinsically complex, with several cooperating and competing phases separated by small energy scales, it is crucial to be able to study very large lattices with different geometries and boundary conditions in order to rule out spurious finite size effects. A useful illustration is found in the one-band Hubbard model, where the magnetic and charge orders in the ground state exhibit long wavelength collective modes which are extremely delicate and sensitive to finite-size effects^{48–50}. The task to systematically determine such orders is especially challenging for many-body approaches, with high computational costs that tend to make it particularly difficult to reliably reach the thermodynamic limit and scan multiple parameters. Mean-field calculations can serve as a valuable guide in this regard. In the one-band Hubbard model, unrestricted Hartree-Fock solutions were found to capture much of the magnetic phase diagram⁵¹, albeit with parameter values that can differ^{32,50}, reflecting the tendency of mean-field theory to exaggerate order.

Although mean-field studies have been performed on the three-band Hubbard model^{3,52–57}, a systematic determination of the magnetic and charge properties within a general mean-field framework is, to our knowledge, still not available. This is the goal of the present work. We employ a generalized Hartree-Fock (GHF) approach which allows non-collinear magnetic orders. As described below, we find a rich ground-state phase diagram, with some phases heretofore not seen in models for cuprates. The phase diagram of the three-band model is much more complex than that of the single-band Hubbard model. Based on the lessons from the single-band model, these phases should serve as very plausible candidate zero-temperature states of the model, possibly with modified parameters (e.g., reduced effective repulsion). The results identify several phases which are potentially important to the physics of the CuO_2 planes in cuprate materials. Our results also provide guidance on finite-size and other subtleties for many-body calculations. The mean-field solution can serve as possible trial wave functions for more advanced quantum Monte Carlo (QMC) investigations.

The rest of the paper is organized as follows. In Sec. II we introduce the three-band Hubbard, or Emery, model. In Sec. III, we outline the GHF method and explain the need, and our strategies, for scanning the parameter space. Sec. IV presents our results in which three distinct phases are observed as Δ is varied: IV A. magnetic domain walls, IV B. spin spirals, and IV C. nematic

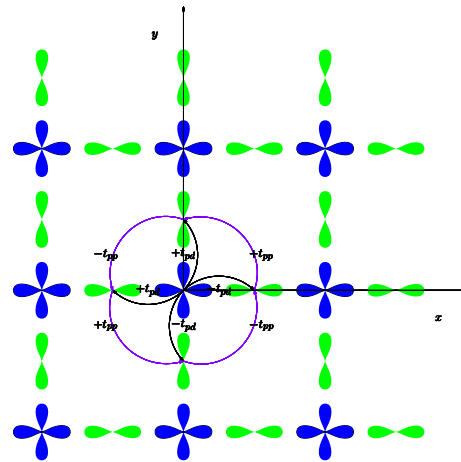


FIG. 1: (Color online) Schematic view of the CuO_2 planes in cuprates. Cu $3d_{x^2-y^2}$ orbitals are represented in blue, and O $2p_x$ and $2p_y$ orbitals in green. We use the reference frame defined by the two axes in the figure. The curve connectors represent the hopping, and the labels define the sign rule.

phases in the intermediate Δ region. We further discuss the results and conclude in Sec. V.

II. MODEL

The Emery model includes the Cu $3d_{x^2-y^2}$ orbital and the O $2p_x$ and $2p_y$ orbitals in the description of the cuprates. In Fig. 1, a schematic representation of the CuO_2 plane is given to help visualize the model. The Hamiltonian is

$$\begin{aligned} \hat{H} = & \varepsilon_d \sum_{i,\sigma} \hat{d}_{i,\sigma}^\dagger \hat{d}_{i,\sigma} + \varepsilon_p \sum_{j,\sigma} \hat{p}_{j,\sigma}^\dagger \hat{p}_{j,\sigma} + \\ & \sum_{\langle i,j \rangle, \sigma} t_{pd}^{ij} \left(\hat{d}_{i,\sigma}^\dagger \hat{p}_{j,\sigma} + h.c \right) + \sum_{\langle j,k \rangle, \sigma} t_{pp}^{jk} \left(\hat{p}_{j,\sigma}^\dagger \hat{p}_{k,\sigma} + h.c \right) \\ & + U_d \sum_i \hat{d}_{i,\uparrow}^\dagger \hat{d}_{i,\uparrow} \hat{d}_{i,\downarrow}^\dagger \hat{d}_{i,\downarrow} + U_p \sum_j \hat{p}_{j,\uparrow}^\dagger \hat{p}_{j,\uparrow} \hat{p}_{j,\downarrow}^\dagger \hat{p}_{j,\downarrow}. \end{aligned} \quad (1)$$

In Eq. (1), i runs over the sites \vec{r}_{Cu} of a square lattice \mathbb{Z}^2 defined by the positions of the Cu atoms. The labels j and k run over the positions of the O atoms, shifted with respect to the Cu sites, $\vec{r}_{\text{O}_x} = \vec{r}_{\text{Cu}} + 0.5\hat{x}$ for the $2p_x$ orbitals, and $\vec{r}_{\text{O}_y} = \vec{r}_{\text{Cu}} + 0.5\hat{y}$ for the $2p_y$ orbitals. This model is formulated in terms of holes rather than electrons: for example, the operator $\hat{d}_{i,\sigma}^\dagger$ creates a hole on the $3d_{x^2-y^2}$ orbital at site i with spin $\sigma = \uparrow, \downarrow$. The first two terms in the Hamiltonian contain the orbital energies, which define the charge-transfer energy parameter $\Delta = \varepsilon_p - \varepsilon_d$, the energy needed for a hole to move from a Cu $3d_{x^2-y^2}$ orbital to an O p orbital. The next two terms describe hopping between orbitals; the hopping amplitudes t_{pd}^{ij} and t_{pp}^{jk} are expressed in terms of two parameters, t_{pd} and t_{pp} , and the dependence on the sites is simply a sign factor, as depicted in Fig. 1. Finally,

Parameter	U_d	U_p	ε_d	ε_p	t_{pd}	t_{pp}
Value (eV)	8.4	2.0	-7.6	-3.2	1.2	0.7

TABLE I: Parameter values adopted in the present study. The parameters are obtained from⁵⁸ La_2CuO_4 . We scan the value of $\Delta = \varepsilon_p - \varepsilon_d$ from 4.4 to 1.5 in our study.

the last two terms represent the on-site repulsion energies, namely double-occupancy penalties similar to those in the one-band Hubbard model. We neglect Coulomb interactions beyond the on-site terms.

As mentioned in the introduction, we study the properties of the model as a function of the charge transfer energy Δ . Our starting point is an *ab initio* set⁵⁸ of parameters obtained for La_2CuO_4 , the parent compound of the lanthanum based family of cuprates. The parameter values are listed in Table I. This set corresponds to a charge transfer energy $\Delta = 4.4$ eV. To correct for possible double counting issues³⁷ would imply a considerable reduction of this value to $\Delta \sim 1.5$ eV. In our calculations we scan the value of Δ in this range. As we will show below, the variation of Δ can dramatically affect the physical properties of the model.

III. METHODS

In order to study the Hamiltonian in Eq. (1), we use a fully self-consistent mean-field approach, where the two-body operators are decoupled as follows:

$$\begin{aligned} \hat{d}_{i,\uparrow}^\dagger \hat{d}_{i,\uparrow} \hat{d}_{i,\downarrow}^\dagger \hat{d}_{i,\downarrow} &\simeq \text{const} \\ &+ \langle \hat{d}_{i,\uparrow}^\dagger \hat{d}_{i,\uparrow} \rangle \hat{d}_{i,\downarrow}^\dagger \hat{d}_{i,\downarrow} + \langle \hat{d}_{i,\downarrow}^\dagger \hat{d}_{i,\downarrow} \rangle \hat{d}_{i,\uparrow}^\dagger \hat{d}_{i,\uparrow} \\ &- \langle \hat{d}_{i,\uparrow}^\dagger \hat{d}_{i,\downarrow} \rangle \hat{d}_{i,\downarrow}^\dagger \hat{d}_{i,\uparrow} - \langle \hat{d}_{i,\downarrow}^\dagger \hat{d}_{i,\uparrow} \rangle \hat{d}_{i,\uparrow}^\dagger \hat{d}_{i,\downarrow}. \end{aligned} \quad (2)$$

The terms in brackets, densities and spin densities, are obtained self-consistently by a diagonalization of a one-body Hamiltonian. We use a generalized Hartree-Fock approach, which constrains only the total number of particles (holes), N .

Since we are interested in the bulk physics of the model, we perform calculations on large lattices, Cu_LO_{2L} hosting N holes corresponding to a doping of $h = N/L - 1$. In order to minimize size effects, which is important if long-range charge or magnetic orders are present, we explore different choices of geometries (square and rectangular supercells) and boundary conditions while keeping h fixed. More precisely we consider both periodic boundary conditions (PBC) and twist boundary conditions (TBC) with random twist angles. We examine both “regular” and tilted supercells. The former has basis vectors along the coordinates axes depicted in Fig. 1, while the latter has basis vectors along the two diagonal directions, i.e., those obtained from rotating the x - and y -axes by $\pi/4$. The tilted supercell requires considering unit cells containing two Copper atoms and four Oxygen

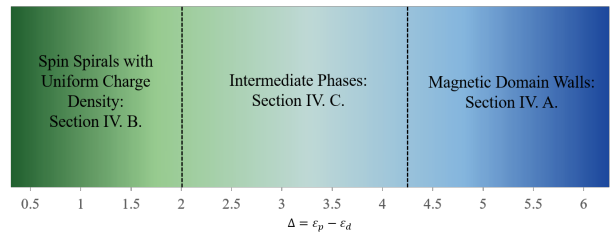


FIG. 2: (Color online) Different phases given by GHF as a function of the charge transfer energy Δ . The phase “boundaries” are meant as rough guides only. Each parameter regime is discussed in a subsection as indicated in the figure.

atoms and is meant to capture orders along the diagonal direction. In both cases, we will use the notation $L_a \times L_b = L$ to denote the dimension of our supercell, with a (b) being either x (y) or the two diagonal directions. We study systems with increasing L to improve the extrapolation to the bulk limit.

For given lattice and number of holes, the GHF solution will be a Slater determinant of spin orbitals:

$$\begin{aligned} |\Psi\rangle &= \prod_{n=1}^N \hat{\phi}_n^\dagger |0\rangle \\ \hat{\phi}_n^\dagger &= \sum_{i=1}^L \sum_{\sigma=\uparrow,\downarrow} \sum_{\alpha=d,p_x,p_y} u_n(i, \alpha, \sigma) \hat{\alpha}_{i,\sigma}^\dagger \end{aligned} \quad (3)$$

that minimizes the energy $\langle \Psi | \hat{H} | \Psi \rangle$ within the manifold of Slater determinants. From the wave function $|\Psi\rangle$, any ground-state property of the model can be computed. The GHF approach allows the number of the spin- \uparrow and spin- \downarrow particles to fluctuate and non-collinear spin orders to develop. No particular order is assumed at the beginning of the calculation. The self-consistent procedure can lead to a local minimum. In our calculations we frequently introduce random noise in the orders and anneal the solution to help the mean-field procedure locate the order corresponding to the global minimum in energy.

IV. RESULTS

Most of our calculations are at doping $h = 1/8$, using the hopping and on-site interaction parameters given in Table I, while scanning the charge-transfer energy Δ , which represents the energy needed to move a hole from a Copper atom to an Oxygen atom. The parameter Δ , via its interplay with hopping amplitudes and on-site Coulomb repulsion, has a direct consequence on the average density of holes at the Cu and O sites: n_d and n_p , respectively. Magnetic resonance experiments¹⁹ are now able to detect the values of n_d and n_p for the different families of cuprates. These results indicate that smaller differences $(n_d - n_p)$, i.e. smaller values of Δ , correspond to higher critical temperature and thus higher superfluid fraction. The anticorrelation between Δ and the

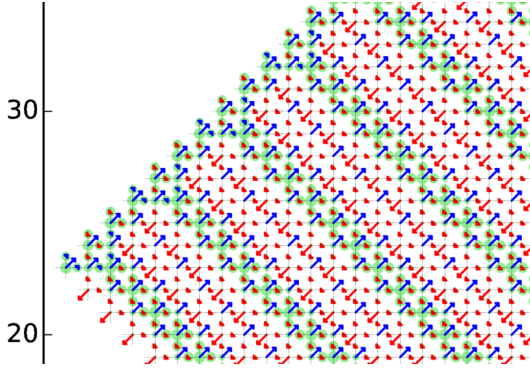


FIG. 3: (Color online) Enlarged section of the magnetic and charge order in the ground state of a 24×30 lattice at $\Delta = 4.4$ eV, $h = 1/8$, and tilted (diagonal) PBC. All spins are aligned or anti-aligned along one (arbitrary) direction in this state. The spin is plotted as red (positive) and blue (negative) arrows, with their length representing the magnitude. The excess hole density given by δn_{excess} is proportional to the size of the green circles.

critical temperature is also seen from scanning tunneling microscopy²². Cluster dynamical mean field theory calculations indicate³⁹ similar tendencies. Thus a systematic investigation of the dependence of the ground-state properties on Δ is especially important and timely.

We find a rich and complex set of possible ground-state magnetic and charge orders as Δ is scanned. At hole doping of $h = 1/8$ and with hopping and on-site repulsion parameters listed in Table I, three different regimes are encountered with GHF as Δ is varied: magnetic domain walls at high Δ (~ 4.4 eV), spiral spin-density waves at low Δ (~ 1.5 eV), and nematic intermediate phases in between. The gradient plot in Fig. 2 shows the parameter range scanned, and these different regimes, which are described separately in the following three subsections.

A. Magnetic Domain Walls (MDWs)

1. Spin and Charge Order at Doping $h = 1/8$

We start from the largest value of the charge-transfer energy, $\Delta = 4.4$ eV. At half-filling, the system is anti-ferromagnetic (AFM) and the densities of holes on the Copper and Oxygen sites are $n_d \approx 0.735$ and $n_p \approx 0.133$, respectively. At doping of $h = 1/8$, the system exhibits diagonal magnetic domain walls (MDW) in the ground state. In Fig. 3 we show the spin and charge densities, using a large supercell, 24×30 , with tilted periodic boundary conditions, i.e., $\text{Cu}_{1440}\text{O}_{2880}$, in order to determine the order. We find that the spins ($S_x(\vec{r})$, $S_y(\vec{r})$, $S_z(\vec{r})$) in the GHF ground state are, to very good accuracy, aligned (anti-aligned) in one arbitrary direction. In the plot we use arrows to represent the spin density, and circles to represent the excess hole density, which we define as:

$$\delta n_{\text{excess}}(\vec{r}) = n_{\text{doped}}(\vec{r}) - n_0(\vec{r}), \quad (4)$$

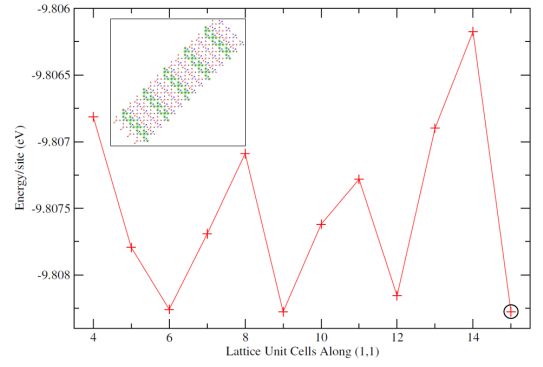


FIG. 4: (Color online) Ground-state energy per site, E/L , vs. supercell size along the diagonal (1,1)-direction for $4 \times L_{(1,1)}$ systems, for $\Delta = 4.4$, $h = 1/8$, tilted PBC. The inset shows the charge and spin order for the lowest E/L solution (corresponding to the 4×15 supercell, indicated by a circle). Magnetic and charge orders are plotted in the same manner as in Fig. 3.

where $n_0(\vec{r})$ is the density at half-filling.

From the plot in Fig. 3, we clearly see an array of lines of increased hole density, with $n_d \approx 0.842$, i.e., extra occupation on the order of $\delta n_{\text{excess}} \sim 0.1$, forming a $\pi/4$ angle with respect to the CuO bonds, superimposed to the AFM background. On the Cu d -sites within these domain wall lines, there is a near perfect spin flip ($\vec{S} \rightarrow -\vec{S}$) creating local ferromagnetic order. These d -sites are surrounded by four O p -sites which also have increased hole occupancy, $n_p \approx 0.225$. The doped holes are concentrated on these lines, with only slight “spill-over” to the adjacent AFM lines. These MDW structures are spaced out and embedded in the rest of the system which is kept essentially at the AFM state found at half-filling. The spin on the O p -sites, negligible at half-filling, remains very small but does show noticeable increase ($\mathcal{O}(10^{-3})$). The small spins on the p -sites are all aligned in the direction opposite to that of the ferromagnetic line defects on the Cu sites (except near the connecting 2-D structures).

The phase of MDWs immersed in an AFM background is suggestive of the stripes found experimentally by Tranquada et. al.¹⁴. However, unlike the stripe states, these domain walls have an overall spin, and the AFM domains separated by the MDWs appear to be in phase. Compared to theoretical studies, the MDW state is reminiscent to the charged Bloch domain lines found in the seminal paper of Zaanen & Gunnarsson³ which studied the SSH model in 2-D, in that excess charge tends to localize on straight lines; however, in the MDW state the domain lines are diagonal, ferromagnetic, and do not induce a phase change across the domain line. Compared to the spiral state found by Assaad⁵² at $U = 6$ and small doping, the MDW state is similar in that they both align along the diagonal (1,1)-direction. However, they differ in their properties. The MDW, in some sense, may combine the presence of AFM spin modulations with ferromagnetism as we will further discuss in IV C.

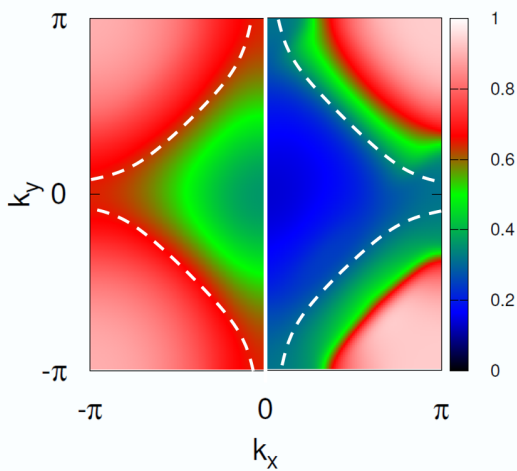


FIG. 5: (Color online) Momentum distribution in MDW state. The total momentum distribution are shown for spin up (left) and spin down (right) particles from the 24×30 supercell calculation of Fig. 3. The white dotted lines outline the Fermi surface of the non-interacting solution for the same system.

Our calculations indicate that the MDWs tend to align periodically in one-dimension (1D) along the diagonal line, though there are some two-dimensional features. We cannot rule out completely that these connecting structures arise solely from commensurability or boundary effects, since we have yet to find a perfectly commensurate lattice that only contains 1D structures. However, a clear preference for a periodicity in spacing is seen in the MDWs. To quantify this feature, we scan long, rectangular lattices. By varying the lattice in a single diagonal direction, minima in the energy/site vs. length will show which geometries are preferred for the domain walls. Fig. 4 shows an example for $4 \times L_{(1,1)}$ lattices. A regular pattern is evident, with minima at $L_{(1,1)} = 6, 9, 12$, and 15. Since there are two copper atoms per unit cell, this corresponds to 12, 18, 24, and 30 diagonal copper planes. This suggests that, at $h = 1/8$, the MDWs prefer lattices that allow regular spacing of 6 copper planes between the domain walls.

Fig. 5 depicts the total spin- \uparrow and spin- \downarrow momentum distributions $n_\sigma(\mathbf{k}) = \langle \Psi | \hat{d}_{\mathbf{k},\sigma}^\dagger \hat{d}_{\mathbf{k},\sigma} + \hat{p}_{\mathbf{k},\sigma}^\dagger \hat{p}_{\mathbf{k},\sigma} | \Psi \rangle$, where $\hat{p}_{\mathbf{k},\sigma}$ is the Fourier transform of $\hat{p}_{j,\sigma}$ with j running over both sets of basis vectors \vec{r}_{O_x} and \vec{r}_{O_y} , and similarly $\hat{d}_{\mathbf{k},\sigma}$ is the Fourier transform of $\hat{d}_{i,\sigma}$. We see the spin imbalance present in the system, as well as the tendency to develop diagonal modulations. Symmetries about the k_x or k_y axes are both broken. In the figure, the left half shows $n_\uparrow(\mathbf{k})$ while the right half shows $n_\downarrow(\mathbf{k})$. The missing portions of the momentum distributions can be constructed by reflection with respect to the origin, $n_\sigma(-\mathbf{k}) = n_\sigma(\mathbf{k})$. In addition to the broken spin symmetry, we see significant re-construction of the Fermi surface to create nesting which produces the modulated MDW structures. We comment in passing that spin imbalance with attractive

interactions, for example in Fermi atomic gases on an optical lattice, are expected to have non-trivial modulated pairing states. It would be interesting to investigate possible relation between the spin imbalance seen here and potential non-trivial pair density wave states, using more advanced many-body methods in future studies.

2. Formation of Domain Walls from Low Doping

To probe the mechanism that leads to the formation of the MDW within the AFM background, we scan lightly doped systems. The plots in Fig. 6 illustrate how a small number of holes accumulate and nucleate. For single hole systems, the calculations show that the extra hole (green circle) localizes around a randomly chosen copper site in a periodic supercell. There is some smearing over to local O sites as well as nearest neighbor copper sites. The system has perfect AFM order on the copper atoms, except for the site where the hole localizes. On that site, there is local ferromagnetic order with neighboring copper sites. The direction of the spin on the neighboring p -bands oppose this ferromagnetic order. This behavior is very robust, and is seen in all our calculations with a single hole under PBC, for all lattice sizes and geometries. We call this local magnetic and charge order a spin flip defect.

We interpret the spin flip defect, in which the extra hole density is accompanied by an overall spin flip on the corresponding Cu site, as a way to gain exchange energy. The density increase within the ferromagnetic defects (see Sec. IV A) makes the total density of the CuO_2 unit cell well above unity (indeed higher than $1 + h$) along the MDW. This renders the AFM state, which avoids double occupancy of the d -sites, less effective. The system then chooses to flip the spin on the d -site and introduce local ferromagnetic order on the Cu sublattice. In order for this exchange energy gain to be efficient, the excess hole has to remain localized around the spin-flipped site, consistent with the numerical results. If these defects can be properly connected along the diagonal line with minimal frustration, the gain in exchange energy is maximized.

When the system is doped with two holes, the ground state under PBC shows three spin flip defects that bind into a diagonal line as can be seen from the local ferromagnetic behavior superimposed on the AFM background. This diagonal line of three spin flips contains all of the extra hole density. We will refer to this as a magnetic line defect from the AFM order. In less energetically favorable systems, two spin flips similar to the ones in the one hole systems were seen. Our calculations on these systems suggested that the single spin flip defects repel each other, and the lowest energy state is reached when they bind into a magnetic line defect occurring over three diagonal Cu sites.

The last system in Fig. 6 has the same doping, $h = 1/36$, as the two-hole doped system just discussed; however, it has a supercell twice the size, thus giving a doping

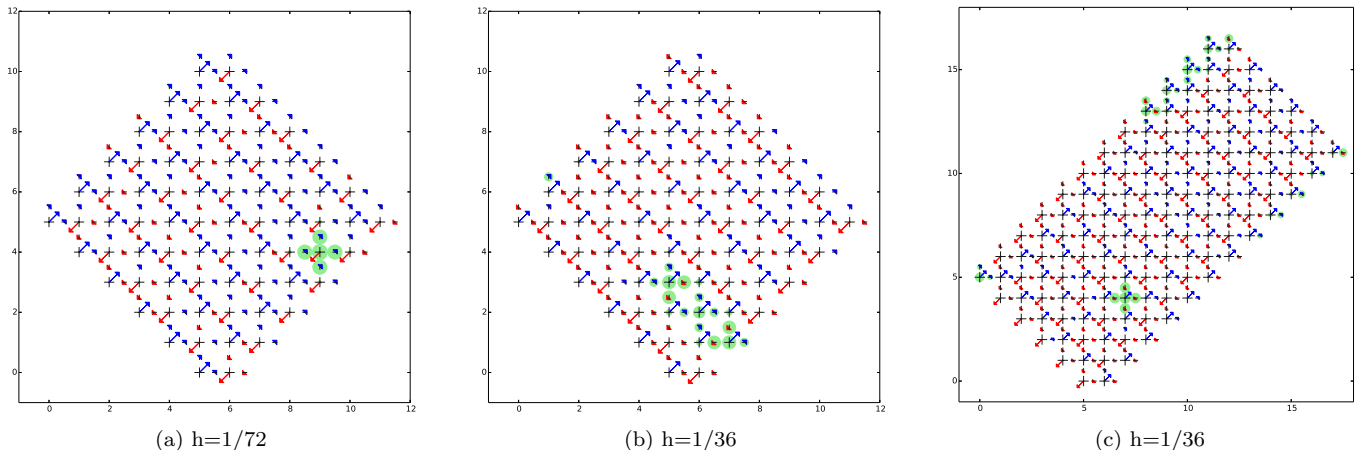


FIG. 6: (Color online) Formation of MDWs from low doping, at $\Delta = 4.4$. The crosses represent the d -orbital on the copper atom and the horizontal and vertical dashes represent the p_x and p_y orbitals on the oxygen, respectively. The colored arrows are proportional to the spin (which are all oriented in one arbitrary direction as in Fig. 3), with blue representing positive spin and red representing negative. The green circles indicate where the extra charge (holes) localize, with their sizes proportional to the excess hole density on a given site (δn_{excess}). Tilted supercells with PBC are used in the calculations, with sizes: a) 6×6 (single hole doped); b) 6×6 (two hole doped); c) 6×12 (four hole doped).

of four holes. The calculations show the magnetic line defects growing longer (5 Cu sites vs. 3) with similar spin and charge order on the O p -sites as the two-hole doped system. Along with the magnetic line defect is an isolated spin flip defect. The calculations suggest that the system slowly builds 1-D magnetic line defects as doping is increased. At first the excess holes repel until a sufficient number of defects are present and it becomes beneficial to combine them. (Pan and Gong⁵³ had performed mean-field studies of a few-hole doped systems, though they did not explore a similar parameter space.)

These calculations suggest the following physical picture from GHF. At very low doping there are isolated holes and short magnetic defect lines. As doping increases, the lines start to create one-dimensional MDWs which are spaced away from each other. Around $h = 1/8$ doping, approaching the maximum superconducting transition temperature, closely spaced, mostly one-dimensional, domain walls dominate the system. As doping is further increased, the system starts to create orthogonal domain walls, eventually creating checkerboard patterns. Some of these features are likely related to the situation in the intermediate Δ regime, which is discussed below in Sec. IV C.

B. Spin Spirals

1. Magnetic and Charge Order

We now turn to the lowest considered charge-transfer energy, $\Delta = 1.5$ eV. In this regime, we find an AFM state at half-filling with $n_d \approx 0.4657$ and $n_p \approx 0.2672$.

At doping of $h = 1/8$, we find a new spin order, characterized by a uniform charge distribution with a long wavelength planar spin spiral. In the GHF ground state, most of the extra charge (holes) are localized on the oxygen p -orbitals, as opposed to the d -orbitals on the Cu sites.

In Fig. 7, we show the spin density ($S_x(\vec{r})$, $S_y(\vec{r})$, $S_z(\vec{r})$) and the excess hole density, $\delta n_{\text{excess}}(\vec{r})$ on a lattice containing 32×36 unit cells with periodic boundary conditions, that is, from a $\text{Cu}_{1152}\text{O}_{2304}$ supercell. The spin on the p -orbitals is negligible and is omitted in the plot. The charge order is uniform across the lattice. The leading spin order is anti-ferromagnetic on the Cu sites; however, the spin is slowly turning in a randomly chosen plane. Unlike in a linear spin-density wave, the spiral has a near constant total spin, S_{tot} .

In the right panel of Fig. 7, an image of the 3-D *staggered* spin density, $(-1)^{x_i+y_i} \vec{S}_i$ is shown along a line cut. The spin rotation is almost perfectly constrained to a plane (i.e., if all spins are translated to a single point, the spin vectors lie in a plane), with the orientation of the plane seemingly random. The projection of a spin spiral onto a single spin orientation, which would be typically how the spins are resolved experimentally, would appear as a linear spin wave or AFM domains. Our results suggest that such structures could be an indication of a more complex three-dimensional spiral behavior.

To estimate the wavelength of the spiral, we investigated the dependence of the energy per site, E/L , on L_y in $4 \times L_y$ supercells. As we show in Fig. 8, there are comparable energy solutions with spiral wavelengths of 7, 8, 9, and 10 Cu sites. The best solutions, as indicated by E/L , occur at $L_y = 36, 72$, which would suggest a spiral

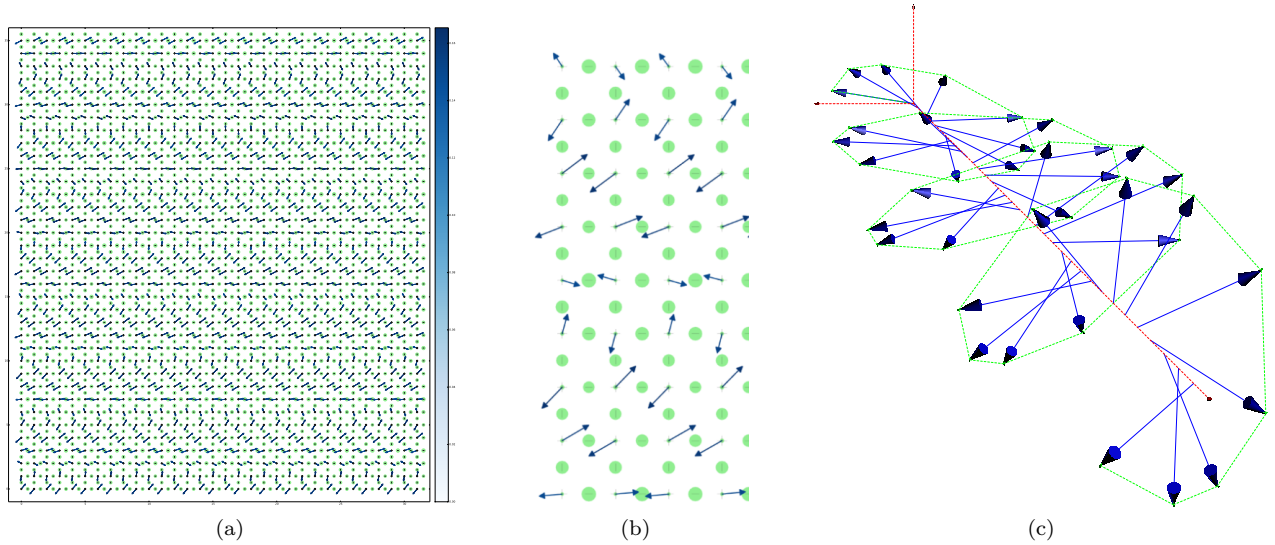


FIG. 7: (Color online) Charge and magnetic order for a periodic 32×36 supercell, with $\Delta = 1.5$ eV and $h = 1/8$. In (a), the spins (arrows) are plotted as a projection in the x - y plane. The total spin, $S_{tot}(\vec{r})$, on each site is given by the color gradient on the right. The spin on the O sites is negligible. The size of the green circles are proportional to the excess hole density from half-filling, $\delta n_{\text{excess}}(\vec{r})$. A small section of the lattice can be seen in (b), better highlighting the order. In (c) a 3-D plot of the staggered spin is shown along a line cut at $x = 0$, viewed along the y -axis. Blue arrows are the real 3D staggered spin and green dashed lines connect near neighbor spins to highlight spiral structure.

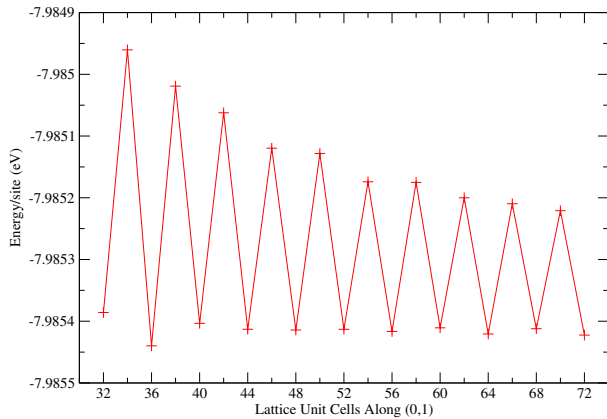


FIG. 8: (Color online) Energy per site vs. lattice length along y for $4 \times L_y$ systems at $\Delta = 1.5$ eV, $h = 1/8$, PBC.

wavelength of 9 Cu sites. On the other hand, perfect spiral order with constant charge order were also observed in an 8×8 supercell. Further, for wider $8 \times L_y$ supercells, the spiral tends to align along the (short) x -direction. We then performed a comprehensive study of 16×18 systems, which shows a variational energy preference to align the spiral in the y -direction ($L_y = 18$) rather than x . This leads us to believe the spiral wavelength is closer to 9

Cu sites, with uniform charge density. The order is very robust against changes in geometries and sizes. The spiral is always oriented along x - or y -direction, propagating along the Cu-O bonds.

2. Momentum Distributions and Nesting

In this section, we examine the properties of the GHF ground state in momentum space. In particular, we are interested in detecting and understanding nesting properties of these systems. As in Sec. IV A 1, we consider spin-resolved momentum distributions $n_{\uparrow}(\mathbf{k})$ and $n_{\downarrow}(\mathbf{k})$. Fig. 9 shows the momentum distributions for a large, 32×36 supercell. Only half of $n_{\sigma}(\mathbf{k})$ is displayed for each σ . In the GHF solution, symmetry is broken along y but preserved in the x direction, so that the full momentum distribution can be recovered by reflection with respect to the k_y axis, $n_{\sigma}(-k_x, k_y) = n_{\sigma}(k_x, k_y)$. The re-construction at the Fermi surface is evident relative to the non-interacting momentum distribution. (It should be stressed that all the formulation is in terms of holes; the momentum distributions for electrons can of course be mapped straightforwardly from these results.)

We observe a spectacular interplay between $SU(2)$ symmetry breaking and translational symmetry breaking, resulting in a nesting property that stabilizes a spin spiral. For perfect AFM order, the nesting vector, \vec{Q} , should coincide with (π, π) . A shift in this nesting vector corresponds to an instability towards a modulated

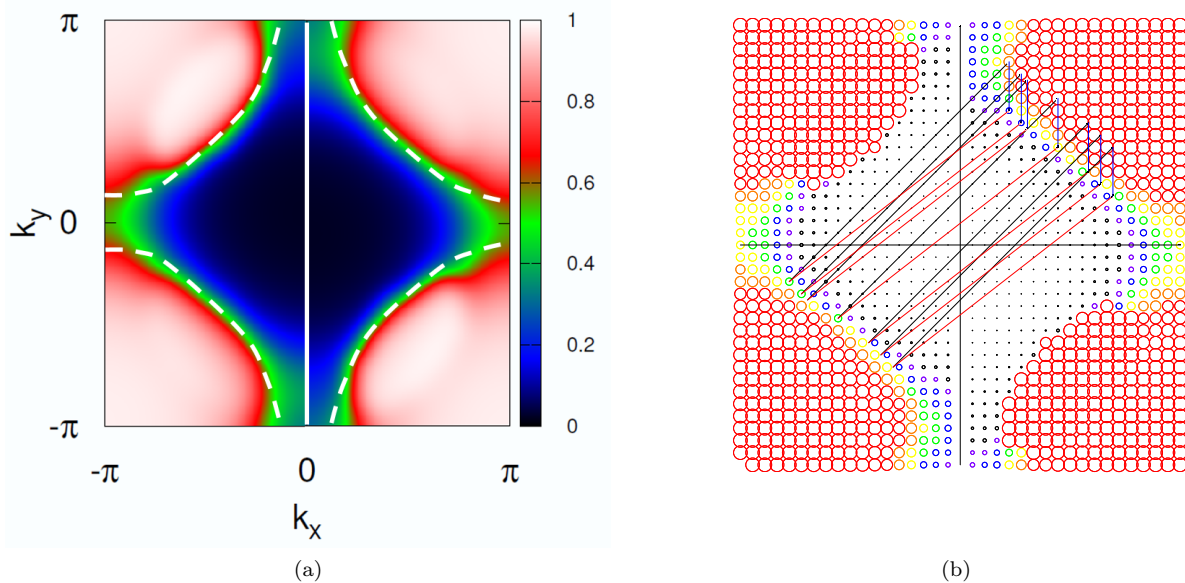


FIG. 9: (Color online) Momentum distribution and nesting structure for spin spiral states. The left panel shows $n_\sigma(\mathbf{k})$ for $\sigma = \uparrow$ (left half) and \downarrow (right half) in the 32×36 supercell in Fig. 7. The color scale is set to show nearly fully occupied momenta in white/red, nearly empty momenta in blue/black, and half occupied momenta around the Fermi surface in green. The white dotted lines outline the Fermi surface of the non-interacting solution for the same system. The right panel illustrates the nesting structure. Similar to the left panel, n_\uparrow is on the left half and n_\downarrow is on the right. The size of the circles is proportional to the occupation (magnitude of n_σ). The colors are to guide the eye around the Fermi surface. The black lines represent a (π, π) vector. The red lines connect complementary points \mathbf{k} and \mathbf{k}' between $n_\uparrow(\mathbf{k})$ and $n_\downarrow(\mathbf{k}')$ near the Fermi surfaces (see text). The blue lines show the shift $(\mathbf{k}' - \mathbf{k})$ [with respect to (π, π)], which defines the spiral wave vector.

phase. In the one-band Hubbard model, for example, the HF solution is found⁵¹ to produce linear spin density waves in large portions of the parameter space, the symmetry $n_\uparrow(\mathbf{k}) = n_\downarrow(\mathbf{k})$ is preserved, and the spin density waves can be thought of as a linear combination of two counter-propagating spirals. Here we have a broken symmetry in the momentum distribution between \uparrow - and \downarrow -spins, resulting in a non-collinear spin wave. The right panel of Fig. 9 illustrates the nesting more quantitatively. We identify complementary points \mathbf{k} and \mathbf{k}' near the two Fermi surfaces for which $n_\uparrow(\mathbf{k}) + n_\downarrow(\mathbf{k}') \doteq 1$ within a few percent. The large number of pairs found indicate that the spiral is created predominantly by a simple pairing mechanism^{51,59} involving two primary planewaves. [The simplest model⁶⁰ to help visualize the spiral state is spin orbitals of the form $u \exp(i\mathbf{k} \cdot \mathbf{r})|\uparrow\rangle + v \exp(i\mathbf{k}' \cdot \mathbf{r})|\downarrow\rangle$, where $|u|^2 + |v|^2 = 1$ and the nesting vector is $\mathbf{Q} \equiv \mathbf{k}' - \mathbf{k}$.] From the figure we see that the nesting vector is consistently shifted along the y -direction by $4 \times (2\pi)/36$, which corresponds to 9 Cu sites in real space. This is consistent with the numerical estimation above.

3. Behavior at Low Doping

We also explored the cases with very low doping (one and two doped holes) in a periodic lattice, as we have done for the magnetic domain wall phase in Sec. IV A 2.

For an 8×8 supercell, $\text{Cu}_{64}\text{O}_{128}$, at $h = 1/64$ and $1/32$ doping, the order of the systems showed very little deviation from half-filling. For a single hole ($h = 1/64$), the calculations show that the order is nearly a perfect antiferromagnet. There are some minor periodic modulations of the total spin in the Cu d -orbitals from an AFM background. The density is also very close to uniform, with minor modulations coinciding with the Cu spin deviation. As in the case of $h = 1/8$, most of the extra density lies on the O p -orbitals. For two holes ($h = 1/32$), the calculations show similar order as the single hole case. The spin shows near perfect AFM order with periodic deviations in the total spin. Compared to the single hole system, the periodic deviation occurs twice as often. The charge order is nearly uniform with most of the extra hole density on the O p -orbitals, again with minor modulation coinciding with that of the total spin.

The low doped regimes for the large ($\Delta = 4.4$) and small charge transfer ($\Delta = 1.5$) systems highlight their differences. In the large charge transfer regime, as discussed in Sec. IV A 2, occupation of the O p -orbital is highly unfavorable compared to occupation of the Cu d -orbital, even at very low doping. This causes the system to find charge configurations in which the extra hole density is concentrated and localized around some Cu sites, where a spin-flip occurs to exploit exchange energy. In contrast, in the lower charge transfer regime, extra holes occupying an O p -site is less unfavorable. This allows

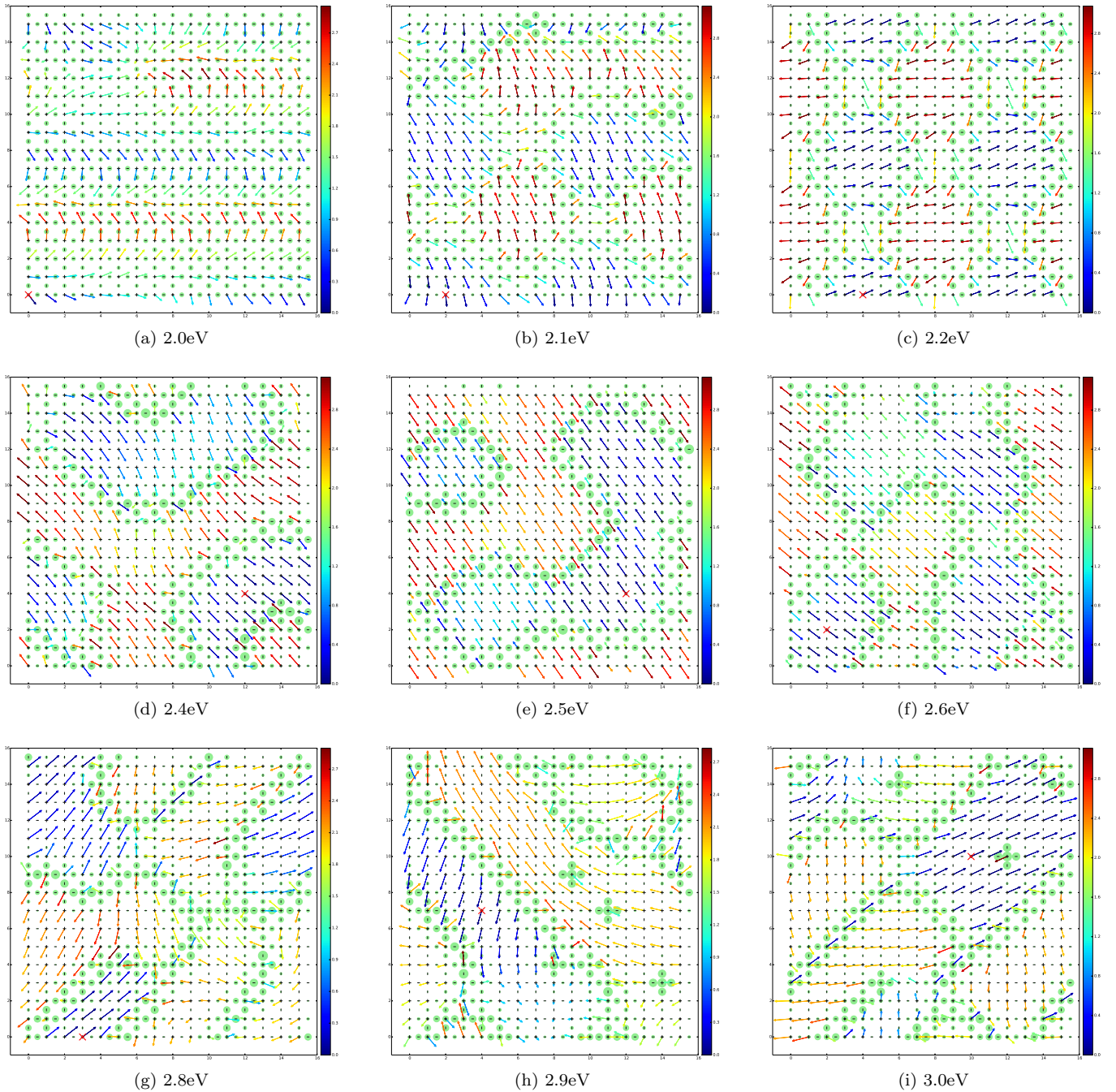


FIG. 10: (Color online) Evolution of the magnetic and charge order from an AFM spiral to ferromagnetic domain walls. A 16×16 supercell is studied for varying values of the charge transfer energy, Δ , in the intermediate regime, at $h = 1/8$. The total staggered spins (arrows) are plotted as a projection in the x - y plane. The color of the arrow represents the angle between the spin on that site and a reference spin marked by the red “x”. It can be thought of as a spin correlation and it runs from $(0, \pi)$. The spin on the O sites is negligible and omitted from the plot. The size of the green circles are proportional to the excess hole density from half-filling, $\delta n_{\text{excess}}(\vec{r})$.

more uniform charge configurations in which the O sites carry most of the excess charge. From the uniformity, the spin order on the Cu sites is able to largely retain AFM order, with smooth modulations leading to wave

behavior (i.e. spin waves and spirals).

C. Intermediate Nematic Order

Within GHF, the MDW phase discussed in Sec. IV A is sustained at high Δ down to $\Delta \sim 4.2$, while the spin spiral phase discussed in Sec. IV B exists up to $\Delta \sim 2$. This is for hole doping of $h = 1/8$ and the parameter values given in Table I. Clearly the phase boundaries in Δ as well as the nature of the phases can vary with the other parameters. We next investigate charge transfer values between the two regimes, scanning $\Delta = 2-3$. Our goal was to determine what happens in the intermediate region between the MDW and the spiral states, whether additional phase(s) exists, and how the transition occurs.

Fig. 10 shows order plots for an $L_x \times L_y = 16 \times 16$ supercell, i.e. $\text{Cu}_{256}\text{O}_{512}$, at $h = 1/8$ for varying values of the charge transfer energy. Systems with $\Delta \leq 2.0$ lie in the spiral phase, while systems with $\Delta \geq 4.3$ lie in the MDW phase. Between the two, there appears to be a crossover regime. Though the charge and spin order are unique at each Δ value as we scan through the transition region, there are common features. At lower values of the charge transfer energy Δ , the excess charge is distributed more uniformly across the O p -orbitals in the lattice. When Δ is raised, the excess charge accumulates into predominantly diagonal lines on the lattice. Up until a sufficient value of $\Delta \sim 2.8$, these lines are mostly centered on the O p -sites. As the charge transfer energy is increased, the lines of excess charge become more rigidly locked at 45° (135°) angles.

Inspecting the spin order in conjunction with the charge order, we also see clearly the effect of doping on the system. Uniform excess holes that lie on the O p -orbitals allow for a smooth spiral modulation of the spin. The system is able to retain anti-ferromagnetism to leading order with an overall modulation to accommodate the excess holes. As the charge starts to accumulate from a uniform distribution to localized diagonal lines, it creates a need for more dramatic changes in the spin order from that at half-filling to accommodate highly localized excess holes. Away from these diagonal lines, the charge order is close to that of half-filling at the same Δ and therefore recovers anti-ferromagnetic order. Close to these lines of excess charge, the spin turns sharply, creating ferromagnetic domain walls that separate spin-isolated anti-ferromagnetic domains.

The excess charge on the Cu atoms leads to a staggered spin correlation between the spin in the neighboring domain and the spin on the domain wall. The value of this staggered spin angle correlation between the two spins seems to be related to the excess hole occupation on the Cu atom. The greater the excess hole occupation, the greater the staggered spin angle correlation is between the domain wall and the neighboring AFM domains. At first, the d -sites develop frustration, i.e., ferromagnetic links, from the AFM background, creating a phase slip similar to the spin-density wave or stripe phase in the one-band Hubbard model⁴⁹⁻⁵¹. As Δ further increases, the Cu sites near the excess charge line start to develop

spin-isolating ferromagnetic domain wall order as a precursor to the MDW phase. Separated by the walls of localized charge density, the AFM order in each isolated domain can be in a completely different direction (third row), creating nematic orders. The spin correlation hits a critical point at a certain excess hole occupation on the Cu atom at which the correlation is at a maximum value of π . For example, when at $\Delta = 3.0$ some of isolated spin flip defects which correspond to this maximum value can be seen. Once the charge transfer energy is high enough ($\Delta \sim 4.3$) to consistently allow greater excess hole occupation on the Cu d -orbitals than the O p -orbitals, we enter the MDW phase, in which the different domains become phase coherent.

Our results in this regime, particularly those regarding the interface between two domains, seems consistent with the spin canting phases found by Seibold et. al, who use an unrestricted Gutzwiller approximation on the three-band Hubbard model^{57,61}. They argue that the spin canting phase is a result of the competition between a classical diagonal stripe phase, characterized by the localized domain walls, and linear spin spirals, characterized by the canting of the spin order near these lines. Though their study finds this order at very low doping of $h = 0.03$, our results are consistent with this interplay between the localized diagonal domain walls and the spin spirals. Unlike this spin canting phase, our nematic phase does not exhibit coherent AFM order in the domains throughout the supercell. Rather, the spiral behavior across different domain walls occurs in different random planes, causing the direction of the AFM order within the domains to isolate from each other, creating the incoherent AFM domains.

V. SUMMARY AND DISCUSSION

We have presented our study of the hole-doped CuO plane applying the generalized Hartree-Fock approach to the three-band Hubbard model. We scanned values of the charge transfer energy and different doping parameters, using “physical” values for the other parameters as derived for lanthanum-based cuprates. We find that, compared to the simplest picture of the one-band Hubbard model, the inclusion of the Oxygen p -orbitals within the three-band (Emery) model leads to new phases with characteristics potentially of direct relevance to experimental observations in high- T_c materials.

The charge transfer energy directly affects the hole occupation on the Cu d -orbitals versus the O p -orbitals. Our study showed that, even for high values of the charge transfer energy ($\Delta = 4.4$), where occupation of the O p -orbitals is highly unfavorable, there is still non-trivial hole occupation on the p -sites, highlighting the importance of the three-band model. Though a majority of the doped holes lie on the Cu d -orbitals, there is significant ordering on near neighbor O p -orbitals. As the charge transfer energy is lowered, more holes occupy the

p -orbitals as expected. At $\Delta = 1.5$ the charge ordering is uniform with a vast majority of the doped holes occupying the O p -orbitals.

While varying the charge transfer energy at doping, $h = 1/8$, we find three distinct phases: Magnetic Domain Walls, Spin Spirals, and an intermediate crossover with nematic order. In the MDW phase, which occurs at large Δ , the doped holes localize on diagonal lines centered on the Cu sites. An overall spin flip ($\vec{S} \rightarrow -\vec{S}$) occurs in the middle along the diagonal line, embedded in an anti-ferromagnetic background. This forms diagonal domain walls with a thickness of three Cu sites along the x (or y) direction, with the middle one bearing the spin flip and most of the excess charge. There is no phase flip between adjacent AFM domains separated by the MDW. Though our lowest energy solutions with finite (but large) supercells tend to show some two-dimensional features, it seems likely that the GHF ground state in the thermodynamic limit is one-dimensional, with parallel diagonal MDWs, with a lateral spacing of 6 Copper sites.

In the spiral phase, which occurs at low $\Delta < 2.0$, the charge order is uniform with most of the doped holes in the O p -orbitals. The spins on the Cu sites have a modulated anti-ferromagnetic order. The anti-ferromagnetic order slowly turns in a randomly chosen plane (depending on the initial variational state) as it propagates along x or y -direction. The wavelength of the spiral, for $h = 1/8$ and with the *ab initio* parameters, appears to be around 8 or 9 Cu sites.

In the intermediate Δ region, there is competition between the uniform charge order of the spiral phase and the localized charge order of the MDW phase. A majority of the doped holes occupy the O p -orbitals. Starting from an antiferromagnetic spiral state propagating along the y -direction (x -direction), the different spiral lines at different y (x) positions gradually develop phase differences beyond the perfect staggered order $(-1)^y$. As the charge transfer energy is increased, holes start to localize on diagonal lines centered on the O p -sites. The spins in the Cu d -orbitals near such O sites make more drastic deviations from the AFM order. As the diagonal lines of

excess charge form, the Cu spin order near it most resembles the linear spin-density wave or stripe order seen in the one-band Hubbard model. The diagonal lines of charge separate anti-phase, anti-ferromagnetic domains.

It is important to keep in mind that these are results from a mean-field GHF approach. More accurate treatment of correlation effects can move the phase boundaries with respect to parameter values (or even invalidate some of the phases). However, experience from the one-band Hubbard model indicates that HF tends to capture most of the magnetic and charge orders qualitatively^{49,51}. In fact in the one-band Hubbard model, UHF with a renormalized effective U/t parameter seems to give quantitatively quite accurate results on the magnetic and charge orders³². Our study serves as a starting point for future studies, and reveals several important candidate phases. For certain advanced methods such as auxiliary-field quantum Monte Carlo (AFQMC), our results also provide the necessary trial wave functions. Furthermore, a self-consistency procedure coupling our GHF calculation to AFQMC will allow an even more accurate determination of the many-body ground state.

It will be very interesting, in future studies, to investigate possible connections of the characteristics of magnetic and nematic orders to superconducting order. This will require more advanced methods, since no superconducting order can arise within the GHF approach adopted here. An approach that generalizes it would be to introduce a term with pairing order in the mean-field Hamiltonian, and couple the calculation self-consistently to a many-body calculation (e.g., AFQMC) to match spin densities and anomalous density matrix (pairing order parameters), which will allow an effective pairing interaction strength to be determined.

We thank the Simons Foundation and NSF (Grant No. DMR-1409510) for their support, High Performance Computing at William & Mary for their resources and help, Henry Krakauer, Enrico Rossi, Mingpu Qin, Peter Rosenberg, and Kyle Eskridge for useful feedback and conversations, and Lucas Wagner for providing us with the parameter values from Table I. The Flatiron Institute is a division of the Simons Foundation.

-
- ¹ M. H. Fischer, S. Wu, M. Lawler, A. Paramekanti, and E.-A. Kim, *New Journal of Physics* **16**, 093057 (2014).
 - ² D. Poilblanc and T. M. Rice, *Phys. Rev. B* **39**, 9749 (1989).
 - ³ J. Zaanen and O. Gunnarsson, *Phys. Rev. B* **40**, 7391 (1989).
 - ⁴ A. J. Millis and M. R. Norman, *Phys. Rev. B* **76**, 220503 (2007).
 - ⁵ S. R. White and D. J. Scalapino, *Phys. Rev. B* **92**, 205112 (2015).
 - ⁶ S. R. White and D. J. Scalapino, *Phys. Rev. Lett.* **80**, 1272 (1998).
 - ⁷ K. Machida, *Physica C: Superconductivity* **158**, 192 (1989).

- ⁸ M. Kato, K. Machida, H. Nakanishi, and M. Fujita, *Journal of the Physical Society of Japan* **59**, 1047 (1990), <https://doi.org/10.1143/JPSJ.59.1047>.
- ⁹ S. Sarker, C. Jayaprakash, H. R. Krishnamurthy, and W. Wenzel, *Phys. Rev. B* **43**, 8775 (1991).
- ¹⁰ A. Thomson and S. Sachdev, *Phys. Rev. B* **91**, 115142 (2015).
- ¹¹ S. R. White and D. J. Scalapino, *Phys. Rev. B* **70**, 220506 (2004).
- ¹² E. Dagotto, *Rev. Mod. Phys.* **66**, 763 (1994).
- ¹³ J. M. Tranquada, AIP Conference Proceedings **1550**, 114 (2013), <https://aip.scitation.org/doi/pdf/10.1063/1.4818402>.

- ¹⁴ J. M. Tranquada, B. J. Sternlieb, J. D. Axe, Y. Nakamura, and S. Uchida, *Nature* **375**, 561 (1995).
- ¹⁵ M. Fujita, H. Hiraka, M. Matsuda, M. Matsuura, J. M. Tranquada, S. Wakimoto, G. Xu, and K. Yamada, *Journal of the Physical Society of Japan* **81**, 011007 (2012), <https://doi.org/10.1143/JPSJ.81.011007>.
- ¹⁶ J. Chang, E. Blackburn, A. T. Holmes, N. B. Christensen, J. Larsen, J. Mesot, R. Liang, D. A. Bonn, W. N. Hardy, A. Watenphul, M. v. Zimmermann, E. M. Forgan, and S. M. Hayden, *Nature Physics* **8**, 871 (2012).
- ¹⁷ R. Comin and A. Damascelli, *Annual Review of Condensed Matter Physics* **7**, 369 (2016), <https://doi.org/10.1146/annurev-conmatphys-031115-011401>.
- ¹⁸ M. Jurkutat, D. Rybicki, O. P. Sushkov, G. V. M. Williams, A. Erb, and J. Haase, *Phys. Rev. B* **90**, 140504 (2014).
- ¹⁹ D. Rybicki, M. Jurkutat, S. Reichardt, C. Kapusta, and J. Haase, *Nature Communications* **7**, 11413 EP (2016), article.
- ²⁰ A. J. Achkar, F. He, R. Sutarto, C. McMahon, M. Zwiebler, M. Hcker, G. D. Gu, R. Liang, D. A. Bonn, W. N. Hardy, J. Geck, and D. G. Hawthorn, *Nature Materials* **15**, 616 (2016).
- ²¹ J. Haase, O. P. Sushkov, P. Horsch, and G. V. M. Williams, *Phys. Rev. B* **69**, 094504 (2004).
- ²² W. Ruan, C. Hu, J. Zhao, P. Cai, Y. Peng, C. Ye, R. Yu, X. Li, Z. Hao, C. Jin, X. Zhou, Z.-Y. Weng, and Y. Wang, *Science Bulletin* **61**, 1826 (2016).
- ²³ C. Weber, C. Yee, K. Haule, and G. Kotliar, *Europhysics Letters* **100**, 37001 (2012).
- ²⁴ P. A. Lee, N. Nagaosa, and X.-G. Wen, *Rev. Mod. Phys.* **78**, 17 (2006).
- ²⁵ N. P. Armitage, P. Fournier, and R. L. Greene, *Rev. Mod. Phys.* **82**, 2421 (2010).
- ²⁶ E. Fradkin, S. A. Kivelson, and J. M. Tranquada, *Rev. Mod. Phys.* **87**, 457 (2015).
- ²⁷ V. J. Emery, *Phys. Rev. Lett.* **58**, 2794 (1987).
- ²⁸ N. P. Armitage, F. Ronning, D. H. Lu, C. Kim, A. Damascelli, K. M. Shen, D. L. Feng, H. Eisaki, Z.-X. Shen, P. K. Mang, N. Kaneko, M. Greven, Y. Onose, Y. Taguchi, and Y. Tokura, *Phys. Rev. Lett.* **88**, 257001 (2002).
- ²⁹ D. Sénéchal, P.-L. Lavertu, M.-A. Marois, and A.-M. S. Tremblay, *Phys. Rev. Lett.* **94**, 156404 (2005).
- ³⁰ P. W. Anderson and R. Schrieffer, *Physics Today* **44** (1991), 10.1063/1.881261.
- ³¹ F. C. Zhang and T. M. Rice, *Phys. Rev. B* **37**, 3759 (1988).
- ³² M. Qin, H. Shi, and S. Zhang, *Phys. Rev. B* **94**, 085103 (2016).
- ³³ S. Sorella, G. B. Martins, F. Becca, C. Gazza, L. Capriotti, A. Parola, and E. Dagotto, *Phys. Rev. Lett.* **88**, 117002 (2002).
- ³⁴ N. M. Plakida, *Condensed Matter Physics*, **5** (2002).
- ³⁵ M. Bejas, A. Greco, and H. Yamase, *Phys. Rev. B* **86**, 224509 (2012).
- ³⁶ S. Sachdev and R. La Placa, *Phys. Rev. Lett.* **111**, 027202 (2013).
- ³⁷ X. Wang, M. J. Han, L. de' Medici, H. Park, C. A. Marianetti, and A. J. Millis, *Phys. Rev. B* **86**, 195136 (2012).
- ³⁸ E. Vitali, A. Chiciak, H. Shi, and S. Zhang, to be published.
- ³⁹ C. Weber, C. Yee, K. Haule, and G. Kotliar, *EPL (Europhysics Letters)* **100**, 37001 (2012).
- ⁴⁰ A. Dobry, A. Greco, J. Lorenzana, and J. Riera, *Phys. Rev. B* **49**, 505 (1994).
- ⁴¹ W. A. Atkinson, A. P. Kampf, and S. Bulut, *New Journal of Physics* **17**, 013025 (2015).
- ⁴² E. Arrigoni, M. Aichhorn, M. Daghofer, and W. Hanke, *New Journal of Physics* **11** (2009), 10.1088/1367-2630/11/5/055066.
- ⁴³ P. R. C. Kent, T. Saha-Dasgupta, O. Jepsen, O. K. Andersen, A. Macridin, T. A. Maier, M. Jarrell, and T. C. Schulthess, *Phys. Rev. B* **78**, 035132 (2008).
- ⁴⁴ G. Dopf, A. Muramatsu, and W. Hanke, *Phys. Rev. B* **41**, 9264 (1990).
- ⁴⁵ R. T. Scalettar, D. J. Scalapino, R. L. Sugar, and S. R. White, *Phys. Rev. B* **44**, 770 (1991).
- ⁴⁶ T. Yanagisawa, S. Koike, and K. Yamaji, *Phys. Rev. B* **64**, 184509 (2001).
- ⁴⁷ M. Guerrero, J. E. Gubernatis, and S. Zhang, *Phys. Rev. B* **57**, 11980 (1998).
- ⁴⁸ C.-C. Chang and S. Zhang, *Phys. Rev. B* **78**, 165101 (2008).
- ⁴⁹ C.-C. Chang and S. Zhang, *Phys. Rev. Lett.* **104**, 116402 (2010).
- ⁵⁰ B.-X. Zheng, C.-M. Chung, P. Corboz, G. Ehlers, M.-P. Qin, R. M. Noack, H. Shi, S. R. White, S. Zhang, and G. K.-L. Chan, *Science* **358**, 1155 (2017), <http://science.sciencemag.org/content/358/6367/1155.full.pdf>.
- ⁵¹ J. Xu, C.-C. Chang, E. J. Walter, and S. Zhang, *Journal of Physics: Condensed Matter* **23**, 505601 (2011).
- ⁵² F. F. Assaad, *Phys. Rev. B* **47**, 7910 (1993).
- ⁵³ L.-H. Pan and C.-D. Gong, *Journal of Physics: Condensed Matter* **18**, 9669 (2006).
- ⁵⁴ G. Seibold, E. Sigmund, and V. Hizhnyakov, *Phys. Rev. B* **48**, 7537 (1993).
- ⁵⁵ G. Seibold, J. Seidel, and E. Sigmund, *Phys. Rev. B* **53**, 5166 (1996).
- ⁵⁶ A. Sadori and M. Grilli, *Phys. Rev. Lett.* **84**, 5375 (2000).
- ⁵⁷ G. Seibold, R. S. Markiewicz, and J. Lorenzana, *Journal of Superconductivity and Novel Magnetism* **26**, 49 (2013).
- ⁵⁸ L. Wagner, private communication.
- ⁵⁹ S. Zhang and D. M. Ceperley, *Phys. Rev. Lett.* **100**, 236404 (2008).
- ⁶⁰ A. W. Overhauser, *Phys. Rev.* **128**, 1437 (1962).
- ⁶¹ G. Seibold, R. S. Markiewicz, and J. Lorenzana, *Phys. Rev. B* **83**, 205108 (2011).